

JGR Solid Earth

RESEARCH ARTICLE

10.1029/2020JB021122

Key Points:

- We investigate crustal deformation caused by Tehri reservoir operations using multi-source geodetic observations
- The elastic crustal response to loading dominates the seasonal ground deformation surrounding the reservoir
- The best-fitting layered elastic model implies a relatively lower effective Young's modulus in the shallow crust during water loading periods

Supporting Information:

Supporting Information may be found in the online version of this article.

Correspondence to:

W. Xu,
wenbin.xu@csu.edu.cn

Citation:

Xie, L., Xu, W., Bürgmann, R., Ding, X., Gahalaut, V. K., & Mondal, S. (2021). Tehri reservoir operation modulates seasonal elastic crustal deformation in the Himalaya. *Journal of Geophysical Research: Solid Earth*, 126, e2020JB021122. <https://doi.org/10.1029/2020JB021122>

Received 4 OCT 2020

Accepted 7 JUL 2021

Tehri Reservoir Operation Modulates Seasonal Elastic Crustal Deformation in the Himalaya

Lei Xie¹ , Wenbin Xu^{2,3} , Roland Bürgmann⁴ , Xiaoli Ding¹ , Vineet K. Gahalaut⁵ , and Saroj Mondal⁵

¹The Department of Land Surveying and Geo-Informatics, The Hong Kong Polytechnic University, Hong Kong, China,

²School of Geosciences and Info-Physics, Central South University, Changsha, China, ³Key Laboratory of Metallogenesis Prediction of Nonferrous Metals and Geological Environment Monitoring (Central South University), Ministry of Education, Changsha, Hunan, China, ⁴Berkeley Seismological Laboratory and Department of Earth and Planetary Science, University of California, Berkeley, CA, USA, ⁵CSIR-National Geophysical Research Institute, Hyderabad, India

Abstract The filling and emptying cycles of reservoir operations may change hydrological mass loading, leading to a flexural deformation of the crust that may compromise the infrastructure safety or trigger earthquakes. In this study, we investigate the seasonal crustal response of the Tehri reservoir in the Garhwal Himalaya, northern India, using interferometric synthetic aperture radar (InSAR), Global Positioning System, the Gravity Recovery and Climate Experiment, radar altimetry, and in-situ water-level measurements. Results show that the evolution of vertical ground deformation is modulated elastically by the reservoir operation, whereas the horizontal displacement measured near the reservoir exhibits a time lag of ~65 days with respect to the vertical displacements and water-level variations. The delayed deformation transients indicate that the reservoir loading/unloading cycles affect the near-surface hydrology in its neighborhood. The broader distribution and higher amplitude of ground deformation during the loading periods revealed by the InSAR time series can be explained by water–rock interactions, which cause a decrease in the effective Young's modulus within the top 300-m crustal layer. Our results demonstrate the potential of using space geodetic data to ensure a better understanding of the solid Earth response to regional hydrological changes.

Plain Language Summary The seasonal variations of water storage in the reservoir alter the stress state and hydrologic loadings in the neighboring region thereby may bring measurable crust deformation at the lakeshore. Recent studies have worked to capture the long-term deformation signals near the reservoirs and lakes, but seldom of them has considered the localized crust behavior on a seasonal scale. To better understand crust deformation processes from this anthropogenic source, we used multiple space geodetic observations, in-situ data, elastic and poroelastic models to study the Tehri reservoir, India. The results show that the ~80 m water loading cycles modulate the elastic deformation close to the reservoir. An asymmetric crustal deformation with higher amplitude and broader impacted area in the loading scenario, providing a possible weakening effect in the fractured shallow crustal medium from the water–rock interaction. While the elastic deformation in the vertical direction is well explained, more complicated horizontal motions may be connected to the local hydrologic conditions.

1. Introduction

The transient variation of mass loading on Earth results in instantaneous elastic ground deformation (Dill & Dobslaw, 2013; Farrell, 1972). Surficial mass changes are mainly influenced by the atmosphere (e.g., atmospheric pressure loading), the oceans (e.g., tidal and non-tidal ocean loading), and the terrestrial hydrosphere (e.g., water storage in surface and near-surface water and snow) (van Dam et al., 2001). The change in inland lake water storage involving substantial mass redistribution provides an opportunity to observe the Earth's crustal response to the transient surface load variation. Conventional ground-based measurements (e.g., leveling) have been used successfully to measure the loading-induced ground deformation (Kaufmann & Amelung, 2000); however, they have a limited spatial coverage and high difficulty in maintaining long-term routine monitoring (B. Liu et al., 2016; Zhang et al., 2020). Space geodetic techniques, including the Global Positioning System (GPS), the Gravity Recovery and Climate Experiment (GRACE), and radar altimetry, can be used to study the potential loading-induced deformation. Elósegui et al. (2003) reported the first evidence

of lake-loading-induced deformation using GPS data near Great Salt Lake, Utah. They found decadal trends of ~ 2 mm/yr in the vertical and ~ 1 mm/yr in the horizontal components at two continuously operating GPS sites within ~ 30 km from the Great Salt Lake owing to the ~ 3 m water variation. However, any potential seasonal variations were unclear and likely included contributions from other sources (e.g., multipath, orbital error, tropospheric model error, draconitic error, and non-tidal atmospheric loading). Saleh et al. (2018) and Wahr et al. (2013) used GPS time series to analyze induced deformation around Lake Shasta, California, and Lake Nasser, Egypt, respectively. Dumka et al. (2018) reported the deformation associated with the filling cycles of four hydroelectric reservoirs in India captured via continuously operating GPS stations. Drawing on a small number of GPS stations near four reservoirs in India, Dumka et al. (2018) found that even a small reservoir (e.g., Dharoi reservoir with a storage capacity of ~ 0.9 km 3) was capable of generating resolvable seasonal deformation (~ 1 cm) near the lake shoreline (i.e., ~ 200 m). However, the major drawback of GPS is that it only allows for point measurements, thus leading to a poor spatial resolution of the deformation field. This makes it difficult to determine the complete deformation pattern caused by the reservoirs' filling and emptying cycles. Similarly, GRACE data are only suitable for capturing large-scale continental hydrological loading given its spatial resolution of >350 km (e.g., Chanard et al., 2014; Fu & Freymueller, 2012).

Reservoir loading-induced crustal deformation can also be captured by satellite interferometric synthetic aperture radar (InSAR). This includes studies of deformation during: (a) rising water periods at Lake Siling Co (Doin et al., 2015) and Lake Bam Co (Li et al., 2012), (b) water withdrawal periods in the Dead Sea (Nof et al., 2012) and Lake Yangzhuoyong (Zhao et al., 2016), and (c) multi-year loading/unloading cycles at Lake Mead (Cavalié et al., 2007) and Toktogul Reservoir (Neelmeijer et al., 2018). Owing to the low temporal resolution of the available InSAR data and the characteristics of natural lake water variations, these prior studies typically focused on long-term changes spanning several years. Only a few current works have studied the seasonal crustal response from lake loading fluctuations. Notably, Gahalaut et al. (2017) and Gahalaut, Gahalaut, et al. (2018) used GPS time series and ALOS-1 PALSAR data spanning a single filling period to study the pattern of seasonal deformation in the Koyna-Warna and Tehri reservoirs.

1.1. Tectonic and Geological Settings of the Study Area

Tehri Lake in Uttarakhand, India, is the reservoir impounded by the Tehri Dam, and its operation began in October 2005. The reservoir has a total storage capacity of ~ 4 km 3 , and its surface area spans ~ 52 km 2 (Gahalaut, Gupta, et al., 2018). The Tehri Dam is a 260.5-m Earth and rock-fill embankment dam and is the highest in Southeast Asia (Kanaujia et al., 2015). It is located on the confluence of the Bhagirathi and Bhilangana rivers, in the Garhwal Lesser Himalaya (Figure 1a) (Gupta & Rajendran, 1986). The exposed rocks near Tehri Lake belong to the Lesser Himalaya sequence including both inner-Lesser Himalaya and outer-Lesser Himalaya units (e.g., Kumaun-Garhwal group, Figure 1b). Near the center of Tehri Lake, we find exposures of the Chandpur formation with phyllite and weathered quartzites. Abundant joints and fractures are exposed in several slopes within the Chandpur formation area (Kumar & Anbalagan, 2016). Other major units near the reservoir are the Nagthat and Rautgara formations which contain phyllites with subordinate quartzites and limestones (Kumar & Anbalagan, 2016; Negi, 1998; Sharma & Prasad, 2018).

Tectonically, the location of Tehri Lake, the Garhwal Himalaya area, has a high potential for large seismic events because accumulating tectonic stress has not been fully released since the $\sim M$ 7.7 1803 earthquake, which occurred somewhere between the India-Tibet border and Devprayag (within 130 km from the Tehri) (Ambraseys & Douglas, 2004; Bilham, 2019; Rajendran et al., 2000). Since the 1990s, two strong earthquakes occurred within 100 km of the reservoir: the 1991 Uttarkashi earthquake (M_w 6.8) and the 1999 Chamoli earthquake (M_w 6.6) (Rajendran et al., 2000; Xu et al., 2016). In addition to three strong-to-major seismic events, small-magnitude earthquakes along the Himalayan seismic belt have occurred close to the Main Central Thrust (MCT) (Figure 1a), which approximately marks the transition from the strongly coupled Main Himalayan Thrust (MHT) in the south to the aseismically creeping MHT to the north (Ader et al., 2012; Dal Zilio, 2020; Stevens & Avouac, 2016). The spatio-temporal distribution of earthquakes within 25 km of the reservoir has shown an apparent change after reservoir impoundment. The International Seismological Centre catalog documents more earthquakes ($3.2 < M_b < 6$) to the north of the reservoir than to its south during the 1967–2004 period, which was before the impoundment (Gahalaut, Gupta, et al., 2018). However, this pattern changed after the impoundment. Both the international and

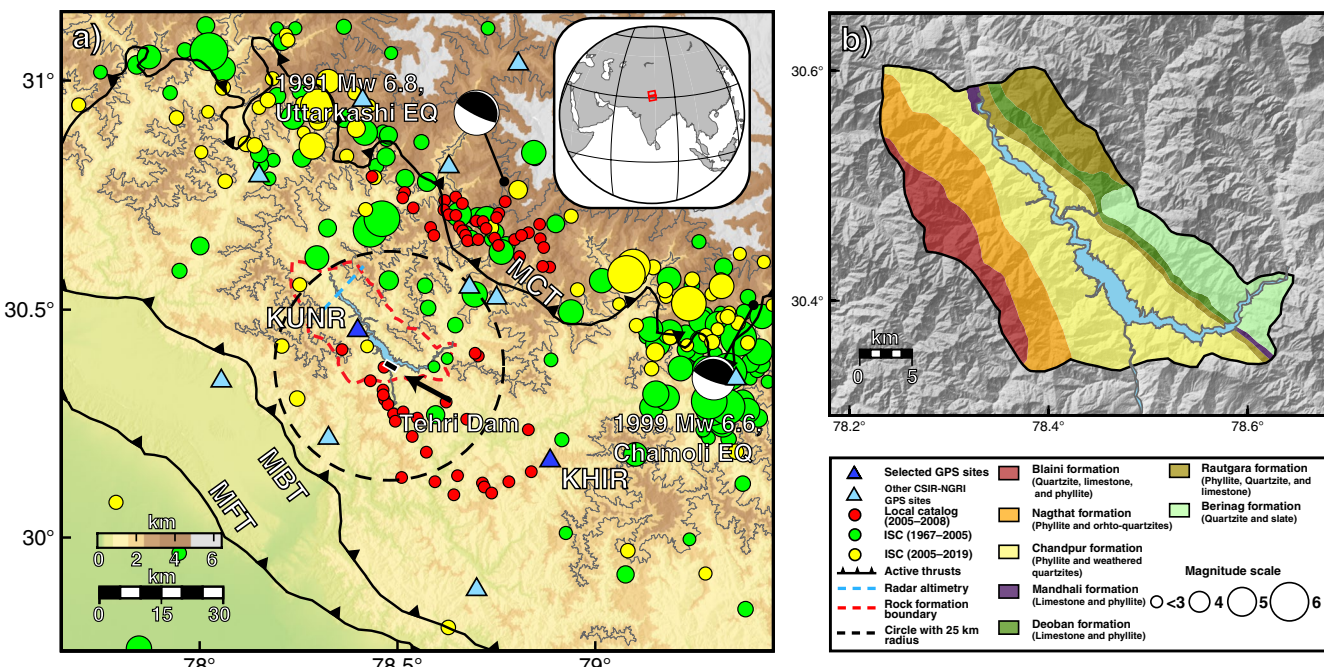


Figure 1. (a) Location of Tehri reservoir with topographic relief around the study area. KUNR and KHUR are two continuously operated Global Positioning System (GPS) sites used in this research, depicted by blue triangles. Other GPS sites operated by CSIR-NGRI, Hyderabad, are depicted by sky blue triangles (Gahalaut et al., 2017). Green and yellow circles represent events ($3.2 < M_b < 6$) from the International Seismological Centre catalog from 1967 to 2005 (pre-impoundment period) and 2005–2019 (post-impoundment period), respectively. Red circles represent earthquakes ($M_w 1.5$ – 2.8) recorded by a temporary network of seismic stations between 2005 and 2008 (Gahalaut, Gupta, et al., 2018; Mahesh et al., 2013). MCT: Main Central Thrust; MBT: Main Boundary Thrust; MFT: Main Frontal Thrust. The sky blue dashed line represents the ground track of the radar altimetry satellite. The black dashed circle denotes the region of a radius of 25 km centered at the Tehri Dam. The dashed red polygon indicates the boundary of detailed geological map in subplot (b). The inset shows the location of the study area. Red rectangles represent the coverage of Sentinel 1A SAR data (ascending track 129, Frames 92 and 97). (b) Geological map of stratigraphy and rocks near the Tehri Lake (Kumar & Anbalagan, 2016; Negi, 1998; Sharma & Prasad, 2018).

regional seismic catalogs show that more earthquakes occurred south of the reservoir (Figure 1a) (Gahalaut, Gupta, et al., 2018; Gupta et al., 2012; Mahesh et al., 2013). Gahalaut, Gupta, et al. (2018) resolved the impoundment-induced Coulomb stress change on the MHT. They suggested that the impoundment of the Tehri reservoir might have inhibited seismicity on the MHT to the north of the dam while decreasing the fault stability on the MHT to the south.

In this study, we combine the Sentinel-1A InSAR time series and GPS data to calculate the crustal response caused by loading variations from the Tehri reservoir and analyze the coupling relationship between the ground deformation and water-level variation (Figure S1). In contrast to previous studies, we focus on the seasonal signals from the reservoir operations and the regional hydrological loading spanning multiple filling cycles. We use a layered-Earth loading model constrained by InSAR observations to explain the response and estimate local elastic rock properties surrounding the reservoir. The remainder of this paper is organized as follows. We describe the data processing steps in Section 2. We model the ground deformation caused by reservoir loading and regional continental hydrological loading in Section 3. The results of the observations and model predictions are reported in Section 4. We discuss the possible causes of ground deformation, inferred regional crust elasticity, and inelastic deformation from the reservoir's loading in Section 5, and summarize our conclusions in Section 6.

2. Data Processing

2.1. Lake Water Level and GRACE Datasets

We used the lake water-level data provided by the Tehri Dam authority, the Central Water Commission of India (CWC), and the United States Department of Agriculture (USDA) to analyze the coupling between

loading variation and the Earth's response. The in-situ measurements were carried out at the Tehri Dam, and the data were provided by the dam authority (2012.6–2015.3) and CWC India (2015.4–2018.1). The USDA data were acquired from a single radar altimetry satellite overpass by Jason-2 (2012.6–2016.9) and Jason-3 (2017.9–2018.1) with a 10-day resolution (Figure S1).

In the Himalaya, the continental hydrological loading cycle caused by variations in terrestrial water storage also generates measurable geodetic deformation (Bettinelli et al., 2008; Chanard et al., 2014; Fu & Freymueller, 2012). This hydrological variation is caused by precipitation from the summer monsoon and seasonal runoff, which depends on the melting or accumulation of mountain snow and glaciers (L. Liu et al., 2019). Therefore, we employed the GRACE-derived RL05 Equivalent Water Height (EWH) product (10-day) from Centre National D'Etudes Spatiales to represent the change in regional-scale terrestrial water storage.

We post-processed the 10-day GRACE EWH time-series product by applying a 30-day window Gaussian filter to suppress the noise and to smooth the time-series data. We removed a linear trend term from the EWH time series to extract the seasonal hydrological loading signals. Subsequently, we modeled the ground displacements caused by regional hydrological loading using the method and the Earth model described in Section 3.1. The observations at the detrended data of far-field GPS site KHIR are closely matched by the model predictions derived from the GRACE EWH with a correlation coefficient of 0.81 and a residual RMS of 0.31 cm in the vertical component (Figure S2, yellow lines). It indicates that the predominant seasonal variation at KHIR site is modulated by the regional hydrological loading. This result is also consistent with findings by Gahalaut et al. (2017), who used the Land Surface Discharge Model to predict the seasonal deformation at KHIR site.

2.2. GPS

A permanent network of 23 continuously operated GPS sites has been deployed to monitor Himalayan crustal deformation in the Garhwal–Kumaun region (Yadav et al., 2019). Two of the sites (Figure 1a), KUNR (30.46°N , 78.40°E ; which is located on the left bank of the Tehri reservoir and KHIR (30.17°N , 78.88°E ; which is located \sim 50 km southeast of KUNR) were used in this study (Dumka et al., 2018; Gahalaut et al., 2017). Both sites are located \sim 60 km northeast of the Main Frontal Thrust. We used the GAMIT/GLOBK software to estimate the coordinates and velocities of the GPS sites from June 2012 to December 2017 and stabilize the solution by incorporating data from core IGS sites (Herring et al., 2010a, 2010b; King & Bock, 2005). We employed the ocean tide model FES2004 to perform the ocean-loading and applied pole-tide corrections (Letellier, 2004). The IERS2003 model was used to correct the effect of solid earth tides at the site locations (McCarthy & Petit, 2004). The Global Mapping Function was used to remove the contribution of the hydrostatic and non-hydrostatic components of the tropospheric delay model (Boehm et al., 2006). The final solution was estimated in the International Terrestrial Reference Frame 2008 (ITRF2008, Altamimi et al., 2011).

The resultant time-series of KUNR and KHIR indicate similar secular velocity in both the north ($v_{\text{N_KUNR}} = 3.47 \text{ cm/yr}$, $v_{\text{N_KHIR}} = 3.45 \text{ cm/yr}$) and east velocity components ($v_{\text{E_KUNR}} = 3.39 \text{ cm/yr}$, $v_{\text{E_KHIR}} = 3.37 \text{ cm/yr}$) (Figure S3). Considering that the seasonal fluctuations at KHIR can be attributed to the regional hydrological loading (Figure S2a, yellow lines) rather than the lake-load induced deformation (less than 1 mm) and the similar geologic, climatic and tectonic environment of these two sites. We therefore used the KHIR site as a reference station to remove contributions from regional hydrological loading at KUNR (Figure 2).

2.3. InSAR

We used Sentinel-1A SAR data from November 2015 to October 2017 in the ascending orbit to study the ground deformation at Tehri reservoir and generate interferograms using the InSAR Scientific Computing Environment software (Agram et al., 2016; Rosen et al., 2012). We did not use the data before November 2015 because of infrequent acquisitions at the beginning of the Sentinel-1 mission. We also did not use the descending-orbit data because they are strongly affected by atmospheric noise and the deformation signal is largely obscured. Because of the rough terrain and dense vegetation near the lake, the InSAR data are affected by spatial and temporal decorrelation that challenge robust interferogram generation (Wei & Sandwell, 2010; Xu et al., 2018). To maximize the signal-to-noise ratio and to extract enough pixels to stabilize the unwrapping procedure, we applied the Stanford Method for Persistent Scatters InSAR time se-

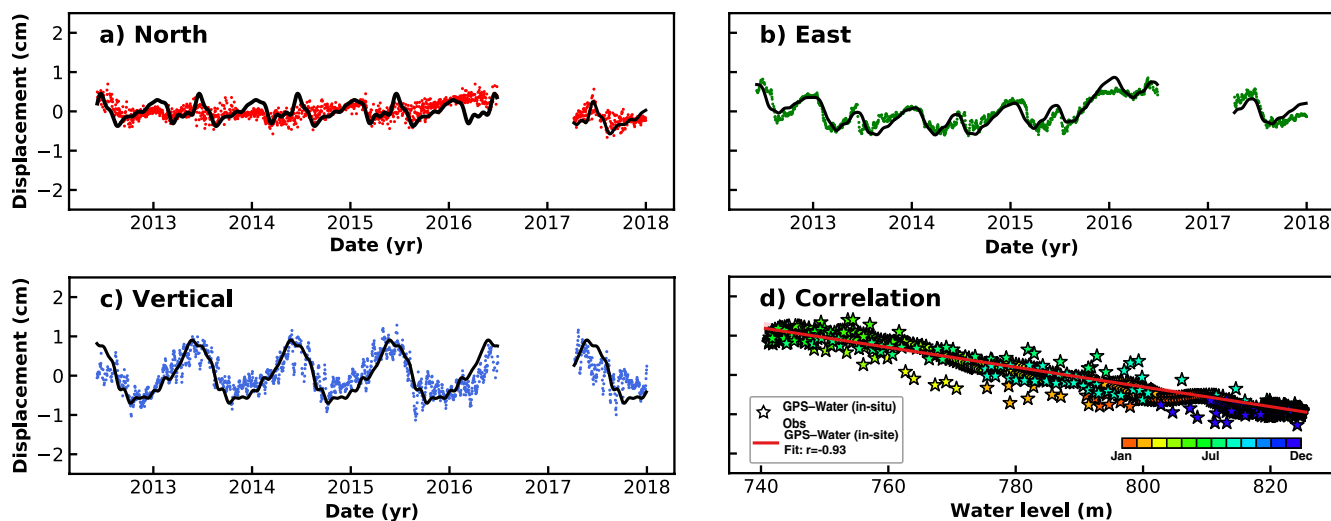


Figure 2. (a–c) Global Positioning System (GPS) time series displacements at station KUNR near Tehri reservoir relative to station KHIR showing seasonal variations in the north, east, and vertical directions, respectively. The black curves represent the best-fitting lines using the Broyden–Fletcher–Goldfarb–Shanno curve fitting method which considering both linear and annual terms (Carpenter et al., 2017). (d) Correlation between the in-situ water-level measurements and the GPS-measured vertical deformation. The GPS data have a gap from July 2016 to March 2017 owing to an instrument malfunction at KHIR station.

ries technique (StaMPS-MTI) to select reliable candidate points and retrieve the small ground deformation (Hooper, 2008). We unwrapped the data iteratively on different unwrapping grid sizes until all interferograms were correctly unwrapped. We removed six noisy interferograms (Figure S4), and all interferograms related to the acquisition from June 29, 2016 in which the phase cannot be unwrapped stably. The final baseline configuration for the InSAR time series analysis is shown in Figure S4. We inverted the unwrapped interferograms to retrieve the line-of-sight (LOS) time series solutions using the least squares method and estimated the spatially correlated topographical errors. To mitigate atmospheric artifacts, we applied the ERA-5 model of the stratified atmospheric delay, which is an hourly atmospheric reanalysis product from Copernicus Climate Change Service Information (Murray et al., 2019; Bekaert et al., 2015). A conventional spatio-temporal filter was used to mitigate atmospheric turbulence. The average residual phase $\hat{\phi}_{\text{resid}}^i = \hat{\phi}^i - \hat{\phi}_{\text{topo}}^i - \hat{\phi}_{\text{atmos}}^i - \hat{\phi}_{\text{deform}}^i - \hat{\phi}_{\text{ramp}}^i$ for all the acquisitions is 3.66 mm (Figure S5a). Although the residual phases may contain residual tropospheric turbulence, uncorrected ionospheric turbulence, remaining decorrelation noise, and other unmodeled signals (Jung et al., 2013; Tong et al., 2013), they exhibit limited correlation to the topography and the atmospheric artifacts are mostly well estimated (Figure S5b). We grouped InSAR-measured ground deformation into four periods of loading (2016.5–2016.9, and 2017.6–2017.10) and unloading (2015.11–2016.5, and 2016.9–2017.6) according to the peak-to-trough water-level time series described in Section 2.3 (Figure 3).

3. Modeling Methods

3.1. Modeling of Reservoir Induced Elastic Ground Deformation

To model the crustal flexure caused by the reservoir operation, we first reconstructed the driving source, mass variation at Tehri reservoir from the in-situ water-level measurements. The surface area of reservoir was discretized into 100×100 m grids. We assigned water-level data and bathymetry to compose the loading cuboids. Because the Shuttle Radar Topography Mission (SRTM) data were acquired before the initial impoundment of Tehri reservoir (Farr et al., 2007), we treated the SRTM DEM as the bathymetry in our model (Figure S6). We then used a layered elastic model (Farrell, 1972; Guo et al., 2004; Longman, 1962) to simulate ground deformation caused by the mass redistribution and constrain the regional depth-dependent rock properties (Young's modulus) using the InSAR data on 30×30 m grids.

To estimate the elastic deformation from reservoir operation on a layered substrate, we defined an appropriate Earth model that includes the elastic moduli and density of multiple layers under a self-gravitating,

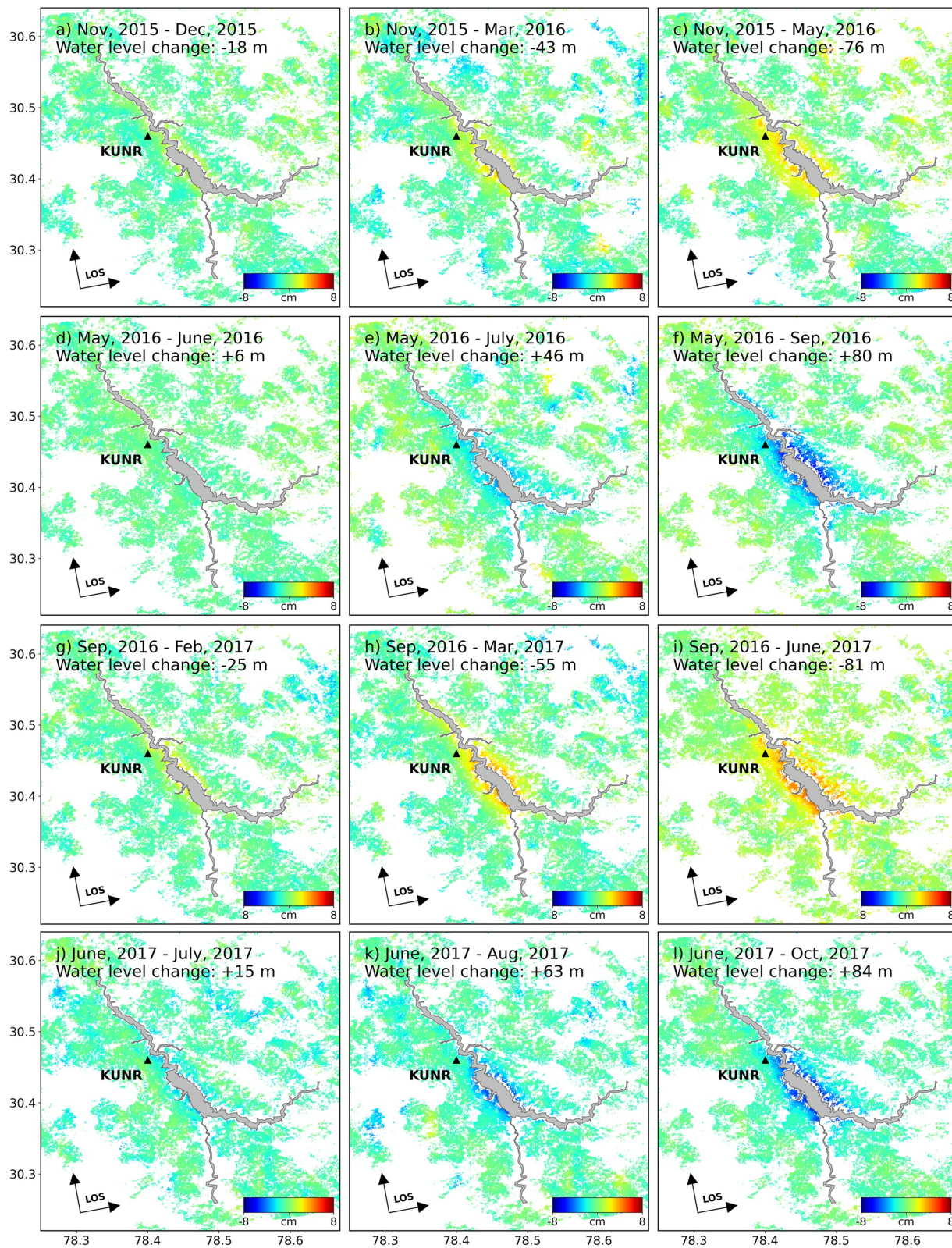


Figure 3. Ground deformation in radar line-of-sight direction between 2015 and 2017. The four rows are divided by peak-to-trough water-level variations. The “warm-colored” points (yellow to red) represent motion toward the satellite (predominantly uplift), and “cold-colored” points (green to blue) indicate motion away from the satellite (i.e., predominantly subsidence). The black triangle in each panel represents the location of Global Positioning System station KUNR.

spherically symmetric, non-rotating, elastic and isotropic Earth model assumption. The Load Love numbers (LLNs), which represent the vertical and horizontal responses of the rigid Earth to the applied external mass are defined as:

$$\begin{aligned} h'_n &= \frac{y_1(R)}{R}, \\ l'_n &= \frac{y_3(R)}{R}, \end{aligned} \quad (1)$$

where y_1 and y_3 are the equations of motion for radial and tangential displacements (Equation 15 from Longman, 1962), and R is the Earth radius. The Load Green's functions (LGFs) for the surface displacements with respect to the unit point mass are then defined as (Farrell, 1972):

$$\begin{aligned} u_\theta &= \frac{R}{m_e} \sum_{n=0}^{\infty} h'_n P_n(\cos\theta) \\ &\approx \frac{Rh_\infty}{m_e} \sum_{n=0}^N P_n(\cos\theta) + \frac{R}{m_e} \sum_{n=0}^N (h_n - h_\infty) P_n(\cos\theta), \\ v_\theta &= \frac{R}{m_e} \sum_{n=1}^{\infty} l'_n \frac{\partial P_n(\cos\theta)}{\partial\theta} \\ &\approx \frac{al_\infty}{m_e} \sum_{n=1}^N \frac{1}{n} \frac{\partial P_n(\cos\theta)}{\partial\theta} + \frac{a}{m_e} \sum_{n=1}^N (nl_n - l_\infty) \frac{1}{n} \frac{\partial P_n(\cos\theta)}{\partial\theta}, \end{aligned} \quad (2)$$

where m_e , R , θ , n , and P_n are the Earth mass, Earth radius, the angular distance from the source to the receiver, the spherical harmonic degree, and Legendre polynomials, respectively. As the results of Equation 2 are from approximations of a high degree LLNs (i.e., a dependence on decomposition of spherical harmonic), we used $N = 5000$ to obtain the asymptotic values of LLNs (Chen et al., 2018; Martens et al., 2019) and the corresponding Green's function (Figure S7). The vertical and horizontal responses of LGFs show that expanding the spherical harmonic to 5,000 degree is sufficient to solve local surface motions (Figure S7). The elastic response of the solid Earth may be affected by a non-planar Earth surface (e.g., Styron & Hetland, 2015); however, here we do not further explore the secondary role of topographic relief in our modeling.

We employed four InSAR deformation maps and grouped them by the water history as loading (Figures 3f and 3l) and unloading data (Figures 3c and 3i) to infer the regional Young's modulus in the 0–15 km. We minimized the misfit between the model predictions and InSAR observations by the grid-search method (Nof et al., 2012; Zhao et al., 2016). We imposed the additional constraint as the elastic moduli increase with depth to avoid fluctuation and unrealistic results. We used the layer information and Young's moduli from seismic waves as initial values (Figure S8, Table S1), and we set the 0–15 km, 0–100 GPa, and 0.1 GPa as the searching ranges of the depth, Young's moduli and search step, respectively.

Since the size and mass change of the Tehri reservoir (i.e., $\sim 40 \text{ km}^2$ and $\sim 2.4 \text{ Gt}$, respectively) are 1–2 orders of magnitude smaller than the loadings from ice-caps (Grapenthin et al., 2006; W. Zhao et al., 2014) or large lakes (Nof et al., 2012; Zhao et al., 2016) (e.g., hundreds of km^2 and tens to hundreds of Gt), the crustal deformation may only reflect the elasticity of the shallow upper crust. To better constrain the depth-dependent elastic heterogeneity in the crust, we performed a depth-sensitivity test following the method in Doin et al. (2015). Starting from a three-layer model (detailed model structure in Figure S9), we separated the elastic model into a 2.5-km layers and decreased Young's modulus in each layer by a factor of 2 (Doin et al., 2015). We compared the difference between the modified model (i.e., half value of the Young's modulus) and the original model as a function of distance to the load center. Although this simple sensitivity test shows that the response is most sensitive to the layers between 5 and 12.5 km depth, the shallowest 0–2.5 km layer also exhibits a substantial response at the near field point that is, 1 km from the reservoir mass center ($\sim 0.6 \text{ cm}$ crustal response, black curves, Figure S9a). The result of our sensitivity test is comparable to that obtained by Doin et al. (2015), which shows the greatest sensitivity of the load field to the elastic parameters at 10–20 km depth at the Siling Co lake.

To further validate whether the elastic properties of the shallowest layer (less than 1 km) can have a significant effect on the near-field elastic loading deformation, we constructed two layered models; a three-layer

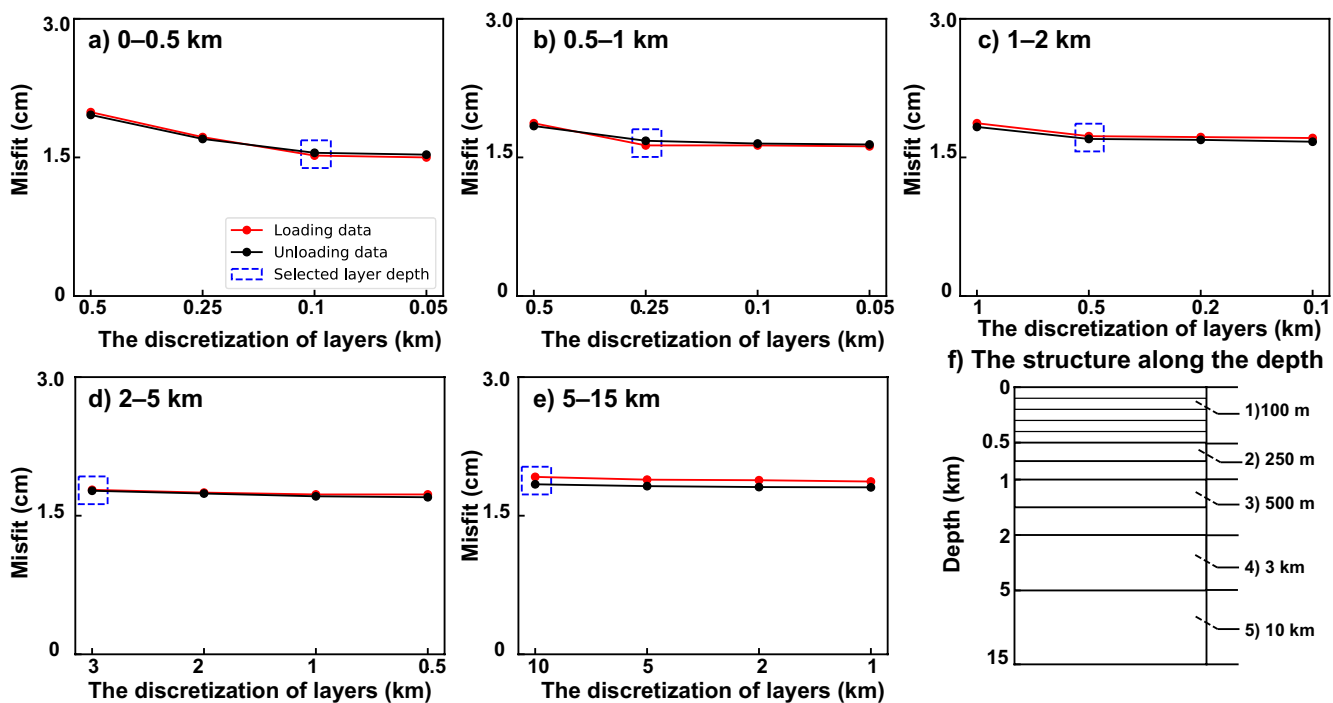


Figure 4. Layer depth discretization: (a–e) Misfits (RMS) from different layer discretization (the stratification in different depth ranges). (f) The selected layer thicknesses are 0.1, 0.25, 0.5, 4, and 10 km in the corresponding depth ranges 1 to 5 (depth is not to scale for improved visualization).

(0–5 km, 5–15 km, and 15–100 km) and a four-layer models (0–1 km, 1–5 km, 5–15 km, and 15–100 km) (Figure S9b). The estimated effective Young's modulus in the four-layer model: 0–1 km is 41.6 GPa, which is 12% lower than the 47 GPa in the 1–5 km layer (Figure S9b, red line) and 8% lower than the 45 GPa in the 0–5 km layer in the three-layer model (Figure S9b, black dashed line). This indicates that the layering in the shallow crust substantially impacts the inferred Young's modulus and can be captured by the elastic model.

Therefore, in order to find the appropriate layering strategy in each layer (i.e., thickness), we quantified the misfits between the observations and model predictions from different stratifications (Figure 4). We first separated the 0–15 km crust into the following five depth ranges: 1) 0–0.5 km, 2) 0.5–1 km, 3) 1–2 km, 4) 2–5 km, and 5) 5–15 km for the reason that the model sensitivity of surface motion and elastic parameters should decrease with depth in the crust. Then, we inverted the elastic parameters in layers of different thicknesses for each depth range, while setting the stratification identical for the other depth ranges. We tested coarser model settings in the shallow depth 0–2 km and found that the coarser models underestimate the near-field deformation, especially in the topmost 0–0.5 km depth (~5 mm; Figure S10), due to the depth-dependent model sensitivity for the local surface loading in the shallow crust. Although we could not exhaustively investigate all the cases, the results suggest an acceptable resolution for the depth discretization as 100, 250, and 500 m in depth ranges 1) to 3), respectively (Figure 4f). To simplify our model, we did not further divide the layers below a 2 km depth, as no substantial improvement was found.

After formulating the layering strategy in the top 15 km, we constrained the Young's moduli separately from both the loading and unloading InSAR data to test whether the elastic rock properties differed during periods of increasing and decreasing compression (Jaeger et al., 2009; Peltzer et al., 1999).

3.2. Modeling of Reservoir Induced Poroelastic Ground Deformation

As opposed to groundwater systems in sedimentary basins, where cm-scale seasonal deformation cycles (uplift and horizontal extension during the wet season) can be observed (e.g., Chaussard et al., 2014; Hu & Bürgmann, 2020), Tehri Lake is located on crystalline basement. Here, we used a coupled poroelastic model (POEL package, Wang & Kümpel, 2003) to model possible contributions in the eastern component of the

GPS time series from the poroelastic rebound induced by subsurface pressure differentials caused by the surface load change. In this poroelastic model, the transport of fluids is assumed to equilibrate the excess pore pressure differentials introduced by surface load changes. The restoration of hydrostatic equilibrium is similar to the pore pressure diffusion process, or poroelastic rebound, which occurs in response to static coseismic pressure changes in the shallow crust (e.g., Peltzer et al., 1999; Zhao, Bürgmann, et al., 2017). Due to the lack of well/piezometric data and regional aquifer system, we do not account for leakage of water from the lake and surface run-off to the underlying rocks, which may change the rock skeleton and cause additional deformation. Therefore, we imposed zero shear tractions at the surface and zero normal displacements and zero excess pore pressure at the bottom of model as the boundary conditions. The hydraulic diffusivity of the porous medium controls the temporal evolution of the pore pressure and associated surface deformation by the following governing equation (Wang & Kümpel, 2003):

$$\begin{aligned} (\lambda + 2\mu)\nabla(\nabla \cdot \mathbf{u}) - \mu\nabla \times (\nabla \times \mathbf{u}) - \alpha\nabla p &= 0, \\ Q^{-1}\frac{\partial p}{\partial t} + \alpha\frac{\partial}{\partial t}\nabla \cdot \mathbf{u} - \chi\nabla^2 p &= q(\mathbf{x}, t), \end{aligned} \quad (3)$$

where \mathbf{u} is the displacement vector, p is the pore pressure changes, λ and μ are the Lamé coefficients, α is the coefficient of effective stress, Q^{-1} is the bulk compressibility, χ is the Darcy conductivity, and $q(\mathbf{x}, t)$ is the loading function with respect to the receiving location and time. We set up the shear modulus according to Young's modulus estimated by the best-fitting layered elastic model (Table S1). The drained/undrained Poisson's ratio and Skempton's coefficient (the change in pore pressure per unit change in confining pressure) were 0.25, 0.35, and 0.65, respectively. Because the fluid flow from loading variation may only be relevant to the uppermost layers at the annual time scale, we set hydraulic diffusivity values ranging from 0.1 to 5 m²/s (i.e., 0.1, 0.5, 1, 2.5, and 5 m²/s) in the first 500 m to evaluate the effect of diffusion velocities on the ground deformation. By defining these five independent parameters, the Biot modulus Q^{-1} (the bulk compressibility), the Biot effective stress α (the change in pore pressure per volumetric unit change in the rock), and Darcy conductivity χ , were uniquely determined. We used the Laplace-Hankel transform method to solve the surface displacements (Wang & Kümpel, 2003).

4. Results

4.1. Seasonal Water-Level Fluctuations at Tehri Reservoir

The in-situ water level gauge indicates a significant seasonal fluctuation of ~80 m associated with the reservoir operations. The in-situ gauge data and radar altimetry data are temporally closely correlated, with a high correlation coefficient of 0.92 and have the same seasonal periodicity (Figure 5). However, there is a ~20 m discrepancy when the water level at the dam site is reduced to the minimum level. This difference may be attributed to the position of the Jason-2/3 ground tracks located upstream of the Tehri Dam (Figure 1a, dashed sky blue line). When the water level decreases to ~760 m (i.e., the minimum water level measured by radar altimetry; green contour in Figure S11), the corresponding along-track lake width is only ~300 m. This is close to the sampling interval of Jason-2/3 altimetry (i.e., ~330 m, Kuo & Kao, 2011). With the continuing decrease of water level to ~740 m (i.e., the minimum water level measured by the in-situ gauge; red contour in Figure S11), the width decreases to ~170 m which is far less than the resolution of radar altimetry. Consequently, the radar altimetry measurement likely involves reflections from the changing topography and other noise when the target surface is reduced to less than the minimum resolution (Gao et al., 2019; Sima & Tajrishy, 2013). Therefore, the altimetry measurement overestimated the water level during lowstand periods, and we relied on the gauge data for our load modeling.

4.2. Seasonal Horizontal and Vertical Deformation at KUNR

The seasonal surface deformation fluctuations with respect to the water history are especially clear in the vertical component of the GPS time series at KUNR. The vertical movement at KUNR shows a strong negative correlation of ~−0.9 with the water-level measurements, suggesting that these two observations are directly coupled (Figures 2d and S12).

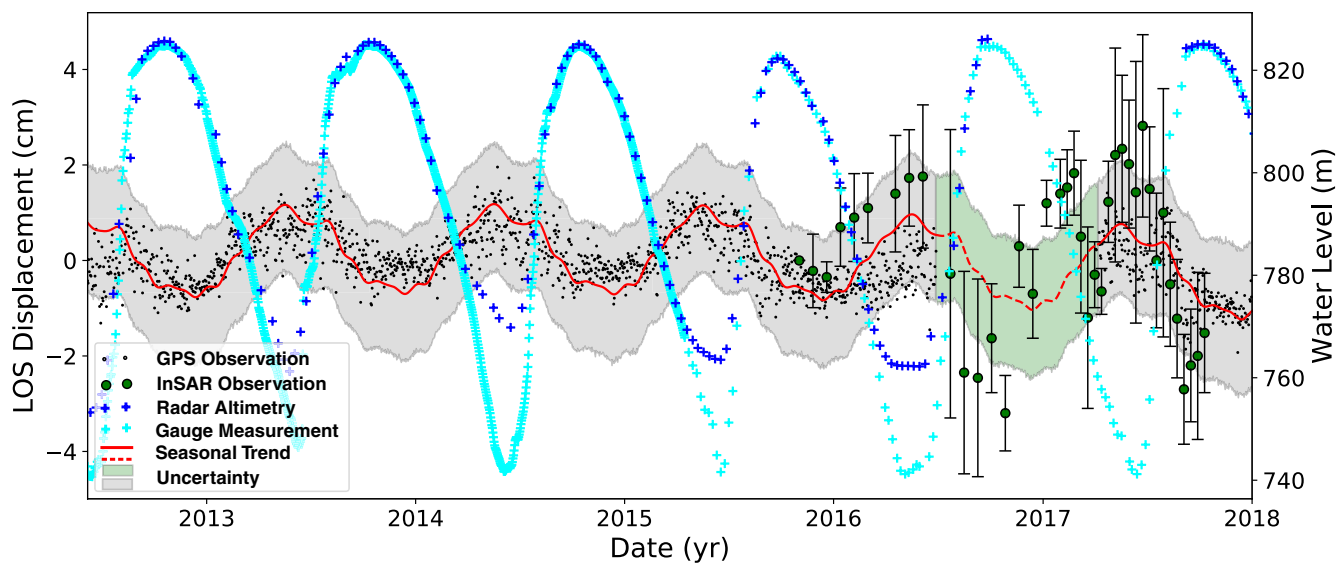


Figure 5. Comparison of Global Positioning System (GPS) (KUNR-KHIR) and interferometric synthetic aperture radar (InSAR) observations (both in the LOS direction) at KUNR site with water level changes from Central Water Commission of India and United States Department of Agriculture at the dam site. The red solid line represents the curve fit to the GPS observations at KUNR (black dots) and its 95% confidence interval (gray shaded area). The dashed red line and green shaded area represent the interpolated GPS observations during the data gap period from July 2016 to March 2017 using Broyden–Fletcher–Goldfarb–Shanno curve fitting. Green circles with error bars represent the InSAR observations estimated from a 15×15 -pixel window around KUNR. The measured water level from (blue cross) radar altimetry and (cyan cross) in-situ gauge measurements are also shown.

The horizontal time series are more complex, as they have two peaks (east component) within a year that are not directly related to the recorded water level changes (north component) (Figure 2). The east component at KUNR station has two seasonal cycles. The larger peaks (with amplitude of ~ 1 cm) in the winter season (October–February) are followed by smaller ones (with amplitude of ~ 0.6 cm) in the summer season (May–August) from 2013 to 2015 (Figure 2b). The observed horizontal movements suggest a periodic variation with an azimuth of $\sim 40^\circ$ (i.e., northwestern to southeastern movements), whereas the elastic model predictions are oriented at $\sim 129^\circ$ (Figure S13, i.e., northeastern to southwestern movements).

4.3. Seasonal Ground Deformation From InSAR Data

The loading and unloading periods show a consistent spatio-temporal ground deformation pattern with the LOS increase and decrease (dominated by the subsidence and uplift, respectively). The magnitude of the surface deformations gradually decreases with the increasing distance from the lakeshore. The associated ground deformation exhibits different behaviors in the following two aspects: (a) the crust in the loading periods appears to produce a stronger response with respect to water-level variation. This leads to an up to ~ 6.6 cm subsidence compared to ~ 5.4 cm of uplift during the unloading periods. (b) The spatial coverage of ground deformation during the loading period is wider than that in the unloading periods. The impacting distance (deformation >3 mm) in the radial direction is ~ 16 km in the loading periods, whereas it is ~ 10 km during the unloading periods.

4.4. Validation

To compare and validate the two independent observations, we projected the 3D GPS time series into the LOS direction. We then simulated the mean seasonal displacement pattern (Figure 5, red dashed curve) of the daily GPS data according to the other five years' observations to fill the gap in the GPS time series between June 2016 and March 2017. We selected InSAR observations in a 15×15 -pixel window near KUNR. Although the InSAR time series showed a larger amplitude than the GPS time series, the projected GPS data somewhat closely matched the InSAR observations, with a correlation of 0.72 and RMS of 0.85 cm. In addition, the InSAR and GPS data showed a strong negative correlation between

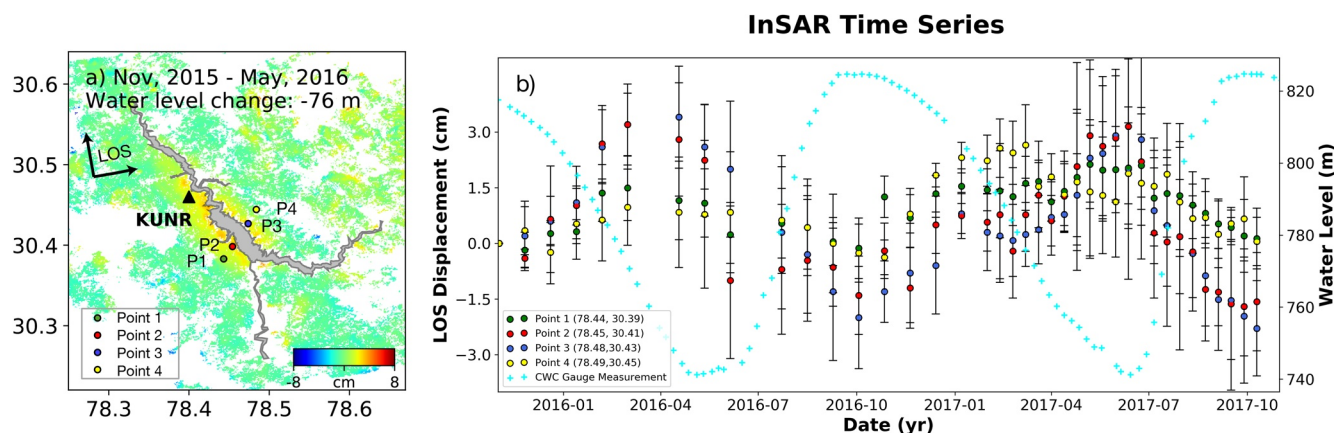


Figure 6. Interferometric synthetic aperture radar (InSAR) time series for four selected points. (a) The layout of selected locations (red and blue points located ~ 0.3 km from the lakeshore; green and yellow points ~ 4 km away). (b) Comparison between InSAR time series at the selected points from November 2015 to October 2017 and gauge water-level measurements.

-0.84 and -0.83 , respectively, with respect to the in-situ water-level measurements. The amplitude and correlation between the temporal and spatial evolution of the surface deformation and mass change decreased with distance from the reservoir (Figure 6). The near-field points (P2 and P3) showed an up to 2 cm response to the water level change, and the negative correlation coefficient reached more than -0.80 . The distant points (P1 and P4) were less affected by the reservoir operation and showed an average correlation of 0.70.

4.5. Deformation Modeling

As discussed in Section 3.1, we modeled the elastic deformation with refined layer structures constrained by the InSAR data (Figure 3). These geodetic models are classified as loading and unloading models (Table S1) using the different InSAR deformation fields according to the loading and unloading periods, respectively.

Surface deformation predictions from both loading and unloading models (Table S1), which are constrained by InSAR data, match closely with the InSAR and GPS observations with misfits at ~ 0.86 and 0.14 cm, respectively. As the crust features a nearly 1 cm additional deformation in the near field during the loading periods (Figures 7 and 8), the inferred deformations from the loading and unloading models also captured the corresponding difference (red and blue dashed lines in Figures 7d, 7h, 8d and 8h). Consequently, the inferred elastic properties from the loading and unloading models substantially differed in the shallow layers. The difference in the upper 1 km is 1.8 GPa per hundred meters and reached as high as 4.1 GPa per hundred meters in the top 300 m (Figure 10b and Table S1). Therefore, we used the optimal Young's modulus in the loading and unloading models separately to fit the InSAR time series data according to the water-level variations. Using this combined model (Table S1), the average fitting error of InSAR data on all time acquisitions decreased from around $0.86\text{--}0.83$ cm, and from 0.14 to 0.12 cm for GPS time series, respectively (Table S1). Comparing the geodetic model predictions with those of the seismic model (Figure S8), we found that the latter significantly underestimated the observed surface deformation during both the unloading and loading periods (Figures 7 and 8).

Although the elastic model fits the InSAR and the vertical component GPS data closely (Figures 9c and 9e), it cannot match the horizontal components of GPS time series. The GPS time series in the east direction shows a bi-annual variation with a secondary peak from May to August, followed by a primary peak from October to February. There is an average delay of 65 days between the peak in the prediction from the preferred elastic loading model and the winter peak in the GPS observations (Figure 9b). Similar to the instantaneous elastic rebound, the added contribution of poroelastic rebounds from different hydraulic diffusivities ($0.1\text{--}5\text{ m}^2/\text{s}$) are relatively small (<0.3 cm, Figure 9c) and does not change the periodicity of simulated elastic deformations. However, in the eastern direction, the pore pressure effects are not superimposed

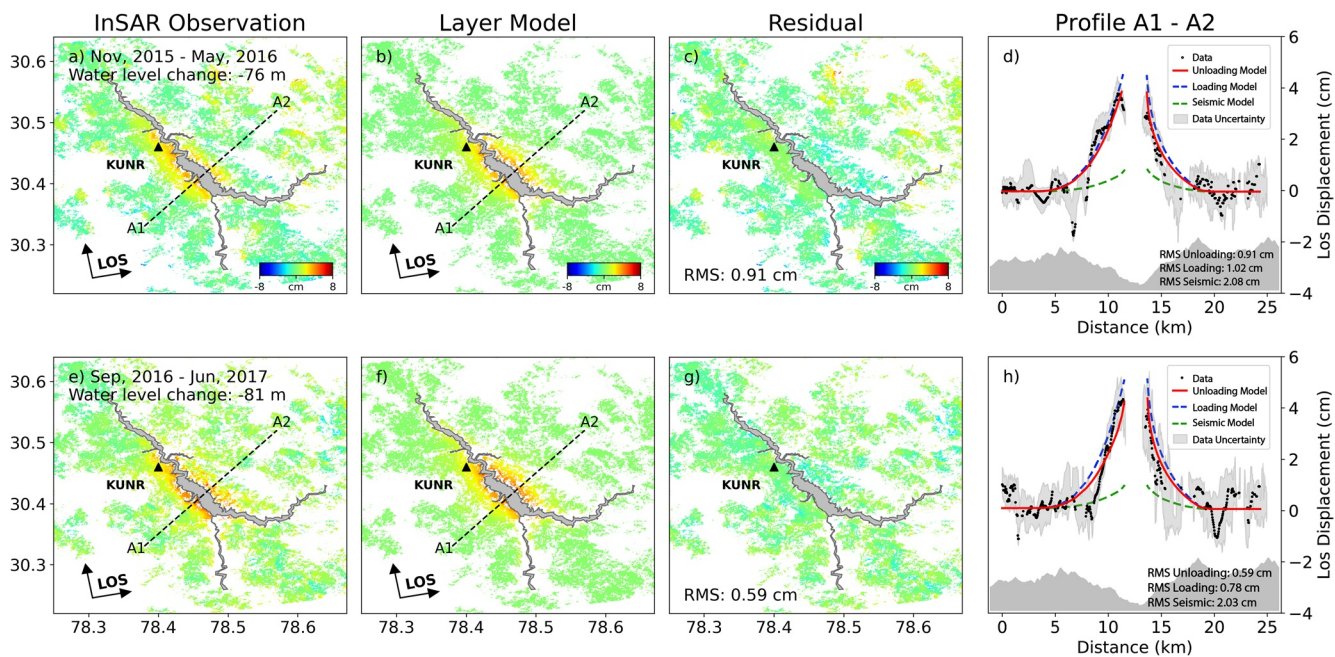


Figure 7. Interferometric synthetic aperture radar (InSAR) unloading observations in comparisons with different model predictions. The first column (a and e): InSAR deformation maps (same as Figures 3c and 3i); Second column (b and f): predictions of the preferred layered elastic model; Third column (c and g): residuals between observations and model estimates; Fourth column (d and h): observed (black) displacements and 1-sigma confidence intervals (gray shading) corresponding to the preferred unloading model (red), loading model (blue), and seismic velocity model (green, see supplementary material) along profiles A1-A2. The topography is plotted at the bottom. The observation periods and water-level change values are indicated in panels (a and e).

by the elastic rebounds and show a substantially delayed signal. The average of the maximum delayed periods between the main peak of the poroelastic model and elastic model is ~ 37 days with a hydraulic diffusivity of $1 \text{ m}^2/\text{s}$ (Figures 9d and 9f: enlarged views in 2014).

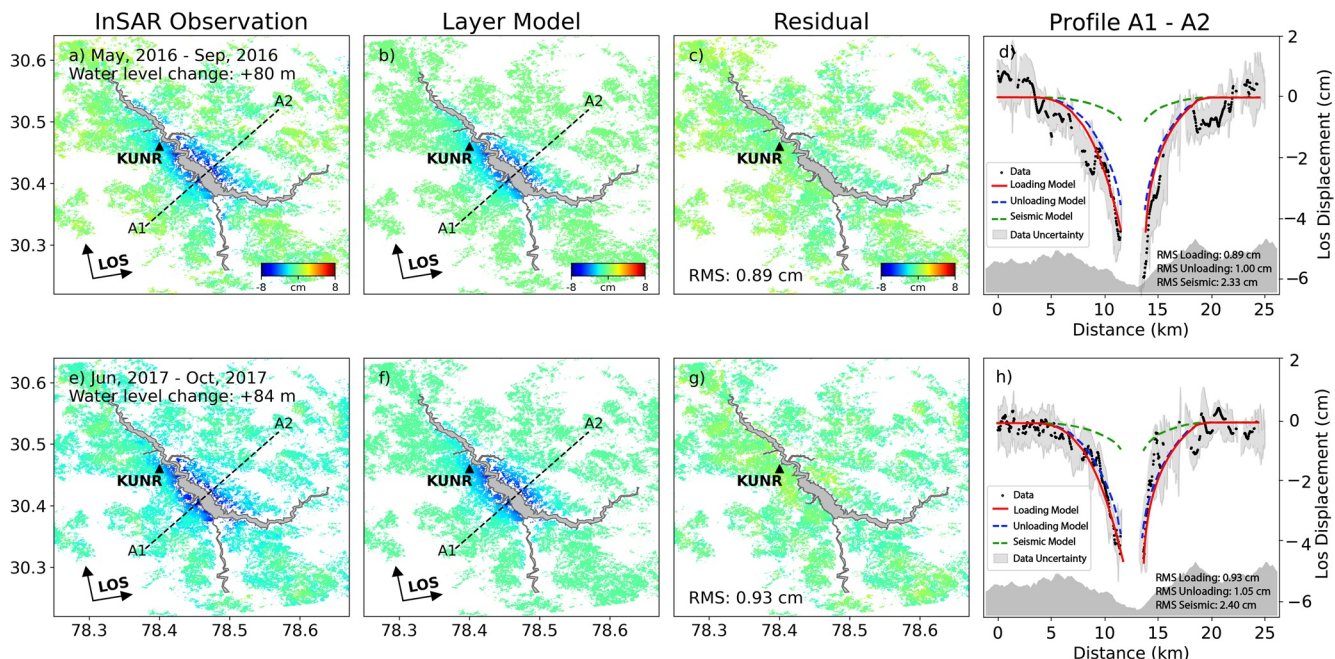


Figure 8. Similar to Figure 7 but for the loading periods of May–September 2016 and June–October 2017. Fourth columns (d and h): red, blue, and green curves represent the preferred model (loading), corresponding unloading model, and seismic velocity model, respectively.

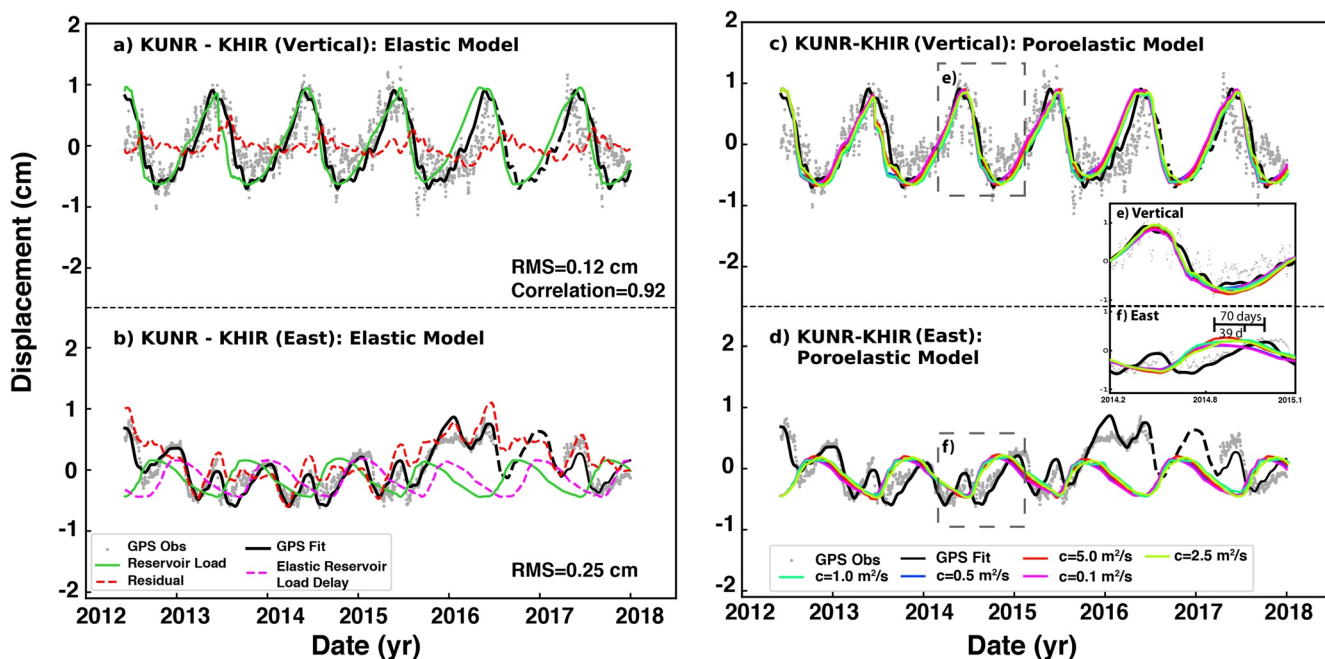


Figure 9. Global Positioning System derived seasonal time series compared with model predictions: (a and b) preferred elastic model (combined models, note that the purple lines represent the model being manually moved by 65 days), and (c and d) poroelastic models considering contributions from the pore pressure effect and elastic deformation, respectively. The hydraulic diffusivities are set from 0.1 to 5 m^2/s in 0–500 m (the zoom-in inset denotes the period from 2014.2 to 2015.1).

5. Discussion

An accurate estimation of elastic parameters is important to understand the rock properties in the crust, which are often difficult to determine from in-situ observations (see supplementary materials for the deformation modeling using seismic data). The existing regional (Gupta et al., 2012) and global seismological models (CRUST 1.0, Laske et al., 2013) represent the first-order elastic structure; however, the coarse resolution in the shallow crust is not suitable for modeling elastic deformation driven by smaller-scale surface loads. Geodetic observations offer an alternative method to estimate the elastic structure of the upper crust and to examine evidence of inelastic processes in the Earth's response to surface loads. In this section, we first discuss the elasticity parameters inferred from InSAR and reference them to the regional seismic results. We then attempt to explain the different deformation patterns during the loading and unloading periods. Finally, we discuss the possible causes of the delayed horizontal GPS time series with respect to the water level.

5.1. Probing Young's Modulus Under Tehri Lake

The strong correlation between the water-level measurement, GPS vertical displacements, InSAR data (Figures 2d and 5), and the layered elastic modeling results (Figures 7 and 8) show that the elastic crustal rebound is responsible for the observed seasonal deformation near the Tehri reservoir. Considering that the exposed rock types near Tehri Lake are phyllite, quartzite, and limestone (Figure 1b; Kumar & Anbalagan, 2016; Negi, 1998; Sharma & Prasad, 2018), the inverted Young's moduli in the shallow crust 0–2 km (7.7–44.2 GPa) are generally comparable to the range of values derived from laboratory experiments, for example, for phyllite the derived estimates are 8.6–17.3 GPa, for quartzite the derived estimates are 36.5–88.3 GPa, while for limestone they are 4.5–89.6 GPa (Zhang, 2017). In addition, our estimation of static Young's modulus at 2–15 km depths from the InSAR time series are close to those derived from the inversion of P- and S- seismic phase data (Gupta et al., 2012, green lines in Figure 10). The 5% difference between the static Young's modulus (i.e., measured from geodetic data) and dynamic Young's modulus (i.e., measured from seismic wave) match closely with that derived in a laboratory set-

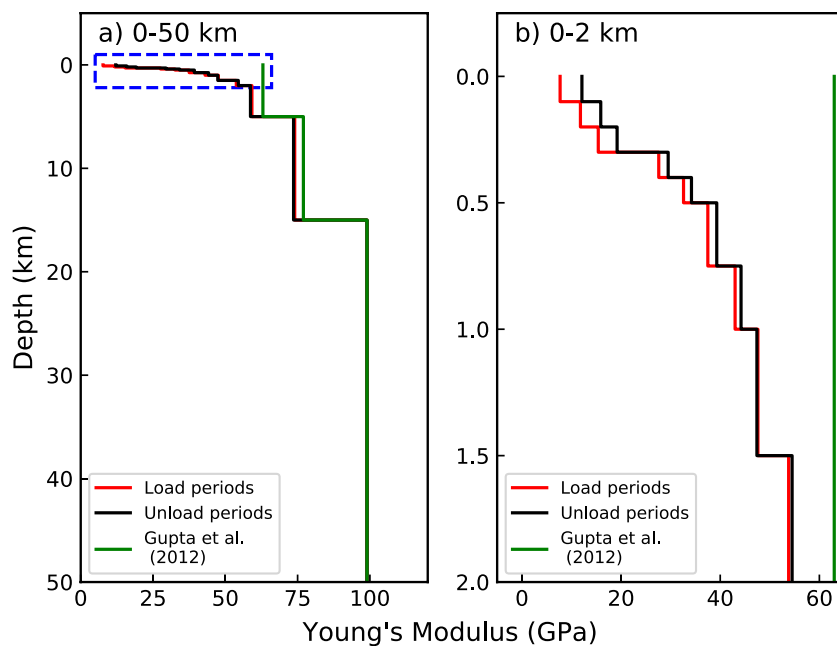


Figure 10. Young's modulus estimated from optimized layered elastic models and seismic velocity profiles (Gupta et al., 2012). (a) 0–50 km (blue dashed rectangle denotes the top 0–2 km shown in b); (b) A close-up view at 0–2 km.

ting (again a 5%–10% variation) (Ciccotti & Mularia, 2004; Davarpanah et al., 2020; Eissa & Kazi, 1988). However, the static Young's modulus is significantly lower in the upper 2 km of the crust because of the following reasons.

1. The presence of cracks and increase in porosity under lower confining pressure in the shallow crust leads to a decrease in the static Young's modulus. Three different laboratory samples: basalt, granite, and tuff, showed a reduction in E_s/E_d (the ratio of static and dynamic elasticity) from 0.90 to 0.65, and 0.75 to 0.30, respectively with a rapid decline in the confining pressure (from hundreds of MPa to tens of MPa) (Adelinet et al., 2011; Cheng & Johnston, 1981). Other geodetic-based inversions from Siling Co Lake, Yangzhuoyong Lake, and Nyiragongo Volcano also reported depth-dependent variations of up to ~75% in the upper crust (Doin et al., 2015; Wauthier et al., 2012; Zhao et al., 2016). Therefore, the reduced value of the obtained Young's modulus in the shallow layers of our model is partly attributed to the presence of cracks and porosity under lower confining pressure.
2. Another possibility is that the micro-crustal structures beneath the Tehri reservoir might have changed because of the repeated lake loading and unloading cycles and associated fluid flow. The existing laboratory experiments show that the rock's effective Young's modulus will be decreased by 44.60% on sedimentary and metamorphic rocks and 33.57% on altered granite after several drained and undrained cycles (Qin et al., 2019; Yang et al., 2018). Therefore, the irreversible decrease in the rock's elastic property caused by the reservoir filling/emptying operation might have contributed to the lower effective Young's modulus in the nearby shallow crust.

5.2. Discrepancy of Deformation Transients Between Un/Loading Cycles

The ground deformation maps in the loading periods show an unexpected stronger crustal response with respect to the water-level change (loading periods: 0.80 mm/m; unloading periods: 0.68 mm/m). This leads to a lower estimation of Young's modulus in the loading periods than in the unloading periods.

As our elastic model is dependent on the reservoir water loading, we further quantified the thermal expansion effects in loading/unloading cycles to exclude the potential perturbation due to the seasonal temperature variations (See Supporting Information S1 and Figure S14 for more details; Tanaka et al., 2001; Wahr

et al., 2014). The resultant slight mass difference (i.e., less than 1%) indicates that the different deformation patterns are not originated from steric errors.

Rock materials commonly exhibit a lower Young's modulus under reduced compressive stress at the same depth of the crust because of the large number of cracks at shallow depths (Jaeger et al., 2009). According to laboratory experiments, the reduction in Young's modulus under tensile stress will range from 10% to 50% (Jaeger et al., 2009; Peltzer et al., 1999). One possible explanation for this unexpected difference is that the water–rock interactions, which weaken the rock's strength, thus playing a definitive role in the shallow crust (Eeckhout, 1976; Zhao, Yang, et al., 2017). Laboratory experiments using different rock samples near other reservoirs (argillite and sandstone from Xu et al., 2008; phyllite from Zhao, Xie, et al., 2017) suggest a reduction in Young's modulus ranging from 28% to 55% during the conversion from unsaturated to saturated conditions. The development of fractures and joints in the rock may decrease the elastic modulus compared to intact rock samples with a decrease ranging between ~10%–70% depending on fracture density (Davy et al., 2018). Therefore, the decrease in Young's modulus at shallow depth beneath the reservoir during the loading periods may be a product of the combined effect of the non-linear elastic properties (i.e., increasing Young's modulus due to the decrease of cracks under a more compressional condition) and the water–rock interaction (i.e., decreasing Young's modulus due to the water weakening effects). Because the difference in loading and unloading periods decays rapidly below 300 m depth, we argue that the impact of water–rock interactions may be concentrated in the upper hundreds of meters under the Tehri reservoir.

5.3. Possible Causes of the Delay in the Peak Eastward Displacement

We found an average delay of 65 days between the peak in eastward motion at GPS station KUNR and the peak water load and vertical displacement. The poroelastic model driving by the fluctuations of reservoir suggests a clear tradeoff between the hydraulic diffusivity and the predicted motion in the east component of the GPS time series (Figure 9d). This is consistent with the time-dependent nature of pore pressure diffusion from fluid flow within the rock, which has a pronounced effect in the near field with a higher diffusion speed. The high-speed transport of fluid quickly dissipates the pore pressure effect according to the diffusion law. The slower diffusion speed causes a larger temporal delay but smaller deformation (Figure 9d, magenta line). The tradeoff between the pore pressure effect and delayed periodicity limits the average maximum deformation delay to ~34–37 days when the hydraulic diffusivity varies between 1 and 2.5 m²/s. Therefore, we argue that the surface deformation from the pore pressure diffusion caused by the surface loading changes can only partially explain the main-peak delay in the east component of GPS.

Since our poroelastic model only takes the pore pressure diffusion process controlled by the reservoir loading into account, we suggest that the pore pressure changes in the local aquifer system from the seasonal surface water (i.e., precipitation and snow melting) and the discharge/recharge of the reservoir may contribute to the abnormal horizontal deformation. Surface water infiltrating into the groundwater by the seasonal run-off and reservoir level contributes to fluctuations of the shallow groundwater level (Oestreicher, 2018). The exposed fractured Chandpur formation near the Tehri Lake may facilitate the water flow through open fissures in the saturated and vadose zones (Sharma & Prasad, 2018). This, in turn, would lead to additional seasonal subsurface pore pressure changes and may cause further rock volume expansions and contractions. In other highly fractured aquifer systems, the shallow groundwater changes have been found to be responsible for altering the transient deformation patterns at millimeter to centimeter levels, especially in the horizontal component (e.g., Devoti et al., 2015; Oestreicher, 2018; Silverii et al., 2016, 2020). However, at the current stage, it is difficult for us to validate physical mechanisms for the abnormal horizontal deformation patterns possibly caused by the localized aquifer or deduce the hydraulic properties due to the lack of regional well data (groundwater level and piezometric data), regional surface run-off, and limited knowledge of local aquifer information (boundary and stratigraphic information).

6. Conclusions

We used space geodetic data and reservoir water-level data to analyze the seasonal ground deformation caused by the Tehri reservoir operation in the Garhwal Himalaya area from 2012 to 2017. Consistent results from different observations and their simulations using a layered elastic Earth model reveal that the Tehri

reservoir modulates the surrounding crustal deformation elastically. We found a different spatio-temporal distribution of crustal response in the loading/unloading periods, which was primarily caused by rock-water interactions in the upper 300 m of the crust. The delayed behavior in the east component of the GPS time series at the KUNR site can be partly explained by the pore pressure effect driven by the reservoir loading variations. In addition to direct pore pressure effect, the abnormal horizontal transients in the GPS time series may also be related to groundwater changes in the regional aquifer from the reservoir operation and seasonal surface run-off. We suggest that future in-situ observations for the local aquifer system and regional surface run-off measurements can help to decipher the physical mechanism in the abnormal transients in the horizontal component. The reservoir loading-induced deformation can help shed new light on the crustal dynamics and the Earth's structure.

Data Availability Statement

Sentinel-1 SAR images were downloaded from the Sentinel-1 Scientific Data Hub (<https://scihub.copernicus.eu>). Water level data were from Dam authority (2012.6–2015.3), Central Water Commission of India (2015.4–2018.1; <http://www.cwc.gov.in/reservoir-level-storage-bulletin>) and the United States Department of Agriculture (2012.6–2018.1; https://ipad.fas.usda.gov/croexplorer/global_reservoir/Default.aspx). GRACE EWH data were from (<https://grace.obs-mip.fr/>). GPS and gauge data can be accessed through (<https://doi.org/10.5281/zenodo.5109718>). Some of the figures were prepared by the Generic Mapping Tools 6.0.

Acknowledgments

We greatly thank the Editor, the Associate Editor and the two reviewers for their thorough constructive comments that greatly helped us to improve our paper. GPS network in the Garhwal Kumaun region is supported by MoES through grant number MoES/P.O.(Seismo)/1(287)/2016). The NGRI publication number of this artical is NGRI/Lib/2021/Pub-81. The research was supported by the National Key R&D Program of China No. 2019YFC1509205 and the National Natural Science Foundation of China under Grant No. 41804015.

References

- Adelinet, M., Fortin, J., & Guéguen, Y. (2011). Dispersion of elastic moduli in a porous-cracked rock: Theoretical predictions for squirt-flow. *Tectonophysics*, 503(1–2), 173–181. <https://doi.org/10.1016/j.tecto.2010.10.012>
- Ader, T., Avouac, J. P., Liu-Zeng, J., Lyon-Caen, H., Bollinger, L., Galetzka, J., & Rajaure, S. (2012). Convergence rate across the Nepal Himalaya and interseismic coupling on the Main Himalayan Thrust: Implications for seismic hazard. *Journal of Geophysical Research*, 117(B4), B04403. <https://doi.org/10.1029/2011jb009071>
- Agram, P. S., Gurrula, E. M., Lavalle, M., Sacco, G. F., & Rosen, P. A. (2016). The InSAR Scientific Computing Environment (ISCE): An Earth Science SAR processing framework, toolbox, and foundry. In *AGU fall meeting abstracts*.
- Altamimi, Z., Collilieux, X., & Métivier, L. (2011). ITRF2008: An improved solution of the international terrestrial reference frame. *Journal of Geodesy*, 85(8), 457–473. <https://doi.org/10.1007/s00190-011-0444-4>
- Ambraseys, N. N., & Douglas, J. (2004). Magnitude calibration of north Indian earthquakes. *Geophysical Journal International*, 159(1), 165–206. <https://doi.org/10.1111/j.1365-246x.2004.02323.x>
- Bekaert, D. P. S., Walters, R. J., Wright, T. J., Hooper, A. J., & Parker, D. J. (2015). Statistical comparison of InSAR tropospheric correction techniques. *Remote Sensing of Environment*, 170(9), 40–47. <https://doi.org/10.1016/j.rse.2015.08.035>
- Bettinelli, P., Avouac, J. P., Flouzat, M., Bollinger, L., Ramillien, G., Rajaure, S., & Sapkota, S. (2008). Seasonal variations of seismicity and geodetic strain in the Himalaya induced by surface hydrology. *Earth and Planetary Science Letters*, 266(3–4), 332–344. <https://doi.org/10.1016/j.epsl.2007.11.021>
- Blilham, R. (2019). Himalayan earthquakes: A review of historical seismicity and early 21st century slip potential. *Geological Society, London, Special Publications*, 483(1), 423–482. <https://doi.org/10.1144/sp483.16>
- Boehm, J., Niell, A., Tregoning, P., & Schuh, H. (2006). Global Mapping Function (GMF): A new empirical mapping function based on numerical weather model data. *Geophysical Research Letters*, 33, L07304. <https://doi.org/10.1029/2005gl025546>
- Carpenter, B., Gelman, A., Hoffman, M. D., Lee, D., Goodrich, B., Betancourt, M., & Riddell, A. (2017). Stan: A probabilistic programming language. *Journal of Statistical Software*, 76(1), 1–32. <https://doi.org/10.18637/jss.v076.i01>
- Cavalié, O., Doin, M. P., Lasserre, C., & Briole, P. (2007). Ground motion measurement in the Lake Mead area, Nevada, by differential synthetic aperture radar interferometry time series analysis: Probing the lithosphere rheological structure. *Journal of Geophysical Research*, 112(B3), B03403. <https://doi.org/10.1029/2006jb004344>
- Chanard, K., Avouac, J. P., Ramillien, G., & Genrich, J. (2014). Modeling deformation induced by seasonal variations of continental water in the Himalaya region: Sensitivity to Earth elastic structure. *Journal of Geophysical Research: Solid Earth*, 119(6), 5097–5113. <https://doi.org/10.1002/2013jb010451>
- Chaussard, E., Bürgmann, R., Shirzaei, M., Fielding, E. J., & Baker, B. (2014). Predictability of hydraulic head changes and characterization of aquifer-system and fault properties from InSAR-derived ground deformation. *Journal of Geophysical Research: Solid Earth*, 119(8), 6572–6590. <https://doi.org/10.1002/2014jb011266>
- Chen, J. Y., Pan, E., & Bevis, M. (2018). Accurate computation of the elastic load Love numbers to high spectral degree for a finely layered, transversely isotropic and self-gravitating Earth. *Geophysical Journal International*, 212(2), 827–838.
- Cheng, C., & Johnston, D. H. (1981). Dynamic and static moduli. *Geophysical Research Letters*, 8(1), 39–42. <https://doi.org/10.1029/gl008i001p00039>
- Ciccotti, M., & Mulargia, F. (2004). Differences between static and dynamic elastic moduli of a typical seismogenic rock. *Geophysical Journal International*, 157(1), 474–477. <https://doi.org/10.1111/j.1365-246x.2004.02213.x>
- Dal Zilio, L. (2020). Bimodal seismicity in the Himalaya controlled by fault friction and geometry. In *Cross-scale modeling of mountain building and the seismic cycle: From Alps to Himalaya* (pp. 67–93). Cham: Springer. https://doi.org/10.1007/978-3-030-28991-1_4
- Davarpanah, S. M., Ván, P., & Vásárhelyi, B. (2020). Investigation of the relationship between dynamic and static deformation moduli of rocks. *Geomechanics and Geophysics for Geo-Energy and Geo-Resources*, 6(1), 1–14. <https://doi.org/10.1007/s40948-020-00155-z>

- Davy, P., Darcel, C., Le Goc, R., & Mas Ivars, D. (2018). Elastic properties of fractured rock masses with frictional properties and power law fracture size distributions. *Journal of Geophysical Research: Solid Earth*, 123(8), 6521–6539. <https://doi.org/10.1029/2017jb015329>
- Devoti, R., Zuliani, D., Braitenberg, C., Fabris, P., & Grillo, B. (2015). Hydrologically induced slope deformations detected by GPS and clinometric surveys in the Cansiglio Plateau, Southern Alps. *Earth and Planetary Science Letters*, 419, 134–142. <https://doi.org/10.1016/j.epsl.2015.03.023>
- Dill, R., & Dobslaw, H. (2013). Numerical simulations of global-scale high-resolution hydrologic crustal deformations. *Journal of Geophysical Research: Solid Earth*, 118(9), 5008–5017. <https://doi.org/10.1002/jgrb.50353>
- Doin, M. P., Twardzik, C., Ducret, G., Lasserre, C., Guillaso, S., & Jianbao, S. (2015). InSAR measurement of the deformation around Siling Co Lake: Inferences on the lower crust viscosity in central Tibet. *Journal of Geophysical Research: Solid Earth*, 120(7), 5290–5310. <https://doi.org/10.1002/2014jb011768>
- Dumka, R., Choudhury, P., Gahalaut, V. K., Gahalaut, K., & Yadav, R. K. (2018). GPS measurements of deformation caused by seasonal filling and emptying cycles of four hydroelectric reservoirs in India. *Bulletin of the Seismological Society of America*, 108(5B), 2955–2966. <https://doi.org/10.1785/0120170355>
- Ekckhout, E. M. (1976). The mechanisms of strength reduction due to moisture in coal mine shales. *International Journal of Rock Mechanics and Mining Sciences & Geomechanics Abstracts*, 13(2), 61–67. [https://doi.org/10.1016/0148-9062\(76\)90705-1](https://doi.org/10.1016/0148-9062(76)90705-1)
- Eissa, A. A., & Kazi, A. (1988). Relation between static and dynamic Young's moduli of rocks. *International Journal of Rock Mechanics and Mining & Geomechanics Abstracts*, 25(6), 479–482. [https://doi.org/10.1016/0148-9062\(88\)90987-4](https://doi.org/10.1016/0148-9062(88)90987-4)
- Elósegui, P., Davis, J. L., Mitrovica, J. X., Bennett, R. A., & Wernicke, B. P. (2003). Crustal loading near Great Salt Lake, Utah. *Geophysical Research Letters*, 30(3), 1111. <https://doi.org/10.1029/2002gl016579>
- Farr, T. G., Rosen, P. A., Caro, E., Crippen, R., Duren, R., Hensley, S., et al. (2007). The shuttle radar topography mission. *Reviews of Geophysics*, 45(2), RG2004. <https://doi.org/10.1029/2005rg000183>
- Farrell, W. E. (1972). Deformation of the Earth by surface loads. *Reviews of Geophysics*, 10(3), 761–797. <https://doi.org/10.1029/rg010i003p00761>
- Fu, Y., & Freymueller, J. T. (2012). Seasonal and long-term vertical deformation in the Nepal Himalaya constrained by GPS and GRACE measurements. *Journal of Geophysical Research*, 117(B3), B03407. <https://doi.org/10.1029/2011jb008925>
- Gahalaut, K., Gupta, S., Gahalaut, V. K., & Mahesh, P. (2018). Influence of Tehri reservoir impoundment on local seismicity of northwest Himalaya. *Bulletin of the Seismological Society of America*, 108(5B), 3119–3125. <https://doi.org/10.1785/0120180077>
- Gahalaut, V. K., Gahalaut, K., Catherine, J. K., Sreejith, K. M., Agrawal, R., Yadav, R. K., et al. (2018). Geodetic constraints on tectonic and anthropogenic deformation and seismogenesis of Koyna-Warna region, India. *Bulletin of the Seismological Society of America*, 108(5B), 2933–2942. <https://doi.org/10.1785/0120170373>
- Gahalaut, V. K., Yadav, R. K., Sreejith, K. M., Gahalaut, K., Bürgmann, R., Agrawa, R., et al. (2017). InSAR and GPS measurements of crustal deformation due to seasonal loading of Tehri reservoir in Garhwal Himalaya, India. *Geophysical Journal International*, 209(1), 425–433. <https://doi.org/10.1093/gji/ggx015>
- Gao, Q., Makhoul, E., Escorihuela, M. J., Zribi, M., Quintana Seguí, P., García, P., & Roca, M. (2019). Analysis of retrackers' performances and water level retrieval over the Ebro river basin using sentinel-3. *Remote Sensing*, 11(6), 718. <https://doi.org/10.3390/rs11060718>
- Grapenthin, R., Sigmundsson, F., Geirsson, H., Arnadóttir, T., & Pinel, V. (2006). Icelandic rhythmites: Annual modulation of land elevation and plate spreading by snow load. *Geophysical Research Letters*, 33(24), L24305. <https://doi.org/10.1029/2006gl028081>
- Guo, J. Y., Li, Y. B., Huang, Y., Deng, H. T., Xu, S. Q., & Ning, J. S. (2004). Green's function of the deformation of the Earth as a result of atmospheric loading. *Geophysical Journal International*, 159(1), 53–68. <https://doi.org/10.1111/j.1365-246x.2004.02410.x>
- Gupta, H. K., & Rajendran, K. (1986). Large artificial water reservoirs in the vicinity of the Himalayan foothills and reservoir-induced seismicity. *Bulletin of the Seismological Society of America*, 76(1), 205–215.
- Gupta, S., Mahesh, P., Sivarao, K., & Rai, S. S. (2012). Active fault beneath the Tehri dam, Garhwal Himalaya-seismological evidence. *Current Science*, 103(11), 1343–1347.
- Herring, T. A., King, R. W., & McClusky, S. C. (2010a). *Documentation of the GAMIT GPS analysis software release 10.4*. Cambridge: Department of Earth, and Planetary Sciences, Massachusetts Institute of Technology.
- Herring, T. A., King, R. W., & McClusky, S. C. (2010b). *GLOBK, Global Kalman filter VLBI and GPS analysis program, version 10.4*. Cambridge: Department of Earth, and Planetary Sciences, Massachusetts Institute of Technology.
- Hooper, A. J. (2008). A multi-temporal InSAR method incorporating both persistent scatterer and small baseline approaches. *Geophysical Research Letters*, 35(16), L16302. <https://doi.org/10.1029/2008gl034654>
- Hu, X., & Bürgmann, R. (2020). Aquifer deformation and active faulting in Salt Lake Valley, Utah, USA. *Earth and Planetary Science Letters*, 547, 116471. <https://doi.org/10.1016/j.epsl.2020.116471>
- Jaeger, J. C., Cook, N. G., & Zimmerman, R. (2009). *Fundamentals of rock mechanics*. John Wiley & Sons.
- Jung, J., Kim, D. J., & Park, S. E. (2013). Correction of atmospheric phase screen in time series InSAR using WRF model for monitoring volcanic activities. *IEEE Transactions on Geoscience and Remote Sensing*, 52(5), 2678–2689.
- Kanaujia, J., Kumar, A., & Gupta, S. C. (2015). 1D velocity structure and characteristics of contemporary local seismicity around the Tehri region, Garhwal Himalaya. *Bulletin of the Seismological Society of America*, 105(4), 1852–1869. <https://doi.org/10.1785/0120144036>
- Kaufmann, C., & Amelung, F. (2000). Reservoir-induced deformation and continental rheology in vicinity of Lake Mead, Nevada. *Journal of Geophysical Research*, 105(B7), 16341–16358. <https://doi.org/10.1029/2000jb900079>
- King, R. W., & Bock, Y. (2005). *Documentation of the GAMIT GPS analysis software*. Massachusetts Institute of Technology.
- Kumar, R., & Anbalagan, R. (2016). Landslide susceptibility mapping using analytical hierarchy process (AHP) in Tehri reservoir rim region, Uttarakhand. *Journal of the Geological Society of India*, 87(3), 271–286. <https://doi.org/10.1007/s12594-016-0395-8>
- Kuo, C. Y., & Kao, H. C. (2011). Retracked Jason-2 altimetry over small water bodies: Case study of Bajhang River, Taiwan. *Marine Geodesy*, 34(3–4), 382–392. <https://doi.org/10.1080/01490419.2011.584830>
- Laske, G., Ma, Z., Masters, G., & Pasquenos, M. (2013). *CRUST 1.0: A new global crustal model at 1 × 1 degrees*.
- Letellier, T. (2004). *Etude des ondes de marées sur les plateaux continentaux, Thèse doctorale, Université de Toulouse III*.
- Li, G., Yang, S., Qiao, X., & Lin, H. (2012). Ground subsidence caused by hydrologic hydrological loading derived by PS-InSAR: Example to Bam Co Lake in Tibetan Plateau. In *33rd Asian Conference on Remote Sensing 2012, ACRS 2012*, 1, 248–256.
- Liu, B., Li, L., Feng, Q., Xie, H., Liang, T., Hou, F., & Ren, J. (2016). Outburst flooding of the moraine-dammed Zhuonai Lake on Tibetan plateau: Causes and impacts. *IEEE Geoscience and Remote Sensing Letters*, 13(4), 570–574. <https://doi.org/10.1109/lgrs.2016.2525778>
- Liu, L., Jiang, L., Jiang, H., Wang, H., Ma, N., & Xu, H. (2019). Accelerated glacier mass loss (2011–2016) over the Puruogangri ice field in the inner Tibetan Plateau revealed by bistatic InSAR measurements. *Remote Sensing of Environment*, 231, 111241. <https://doi.org/10.1016/j.rse.2019.111241>

- Longman, I. (1962). A Green's function for determining the deformation of the Earth under surface mass loads: 1. Theory. *Journal of Geophysical Research*, 67(2), 845–850. <https://doi.org/10.1029/jz067002p00845>
- Mahesh, P., Rai, S. S., Sivaram, K., Paul, A., Gupta, S., Sarma, R., & Gaur, V. K. (2013). One-dimensional reference velocity model and precise locations of earthquake hypocenters in the Kumaon–Garhwal himalaya. *Bulletin of the Seismological Society of America*, 103(1), 328–339. <https://doi.org/10.1785/0120110328>
- Martens, H. R., Rivera, L., & Simons, M. (2019). LoadDef: A Python-based toolkit to model elastic deformation caused by surface mass loading on spherically symmetric bodies. *Earth and Space Science*, 6(2), 311–323. <https://doi.org/10.1029/2018ea000462>
- McCarthy, D. D., & Petit, G. (2004). *IERS tech. Note 32*. Frankfurt am Main, German: Verl. des Bundesamtes für Kartogr. und Geod.
- Murray, K. D., Bekaert, D. P., & Lohman, R. B. (2019). Tropospheric corrections for InSAR: Statistical assessments and applications to the Central United States and Mexico. *Remote Sensing of Environment*, 232, 111326. <https://doi.org/10.1016/j.rse.2019.111326>
- Neelmeijer, J., Schöne, T., Dill, R., Klemann, V., & Motagh, M. (2018). Ground deformations around the Toktogul Reservoir, Kyrgyzstan, from Envisat ASAR and Sentinel-1 Data—A case study about the impact of atmospheric corrections on InSAR time series. *Remote Sensing*, 10(3), 462. <https://doi.org/10.3390/rs10030462>
- Negi, S. S. (1998). *Discovering the Himalaya* (Vol. 1). Indus Publishing.
- Nof, R. N., Ziv, A., Doin, M. P., Baer, G., Fialko, Y., Wdowinski, S., et al. (2012). Rising of the lowest place on Earth due to Dead Sea water-level drop: Evidence from SAR interferometry and GPS. *Journal of Geophysical Research*, 117(B5), B05412. <https://doi.org/10.1029/2011jb008961>
- Oestreicher, N. (2018). *Geodetic, hydrologic and seismological signals associated with precipitation and infiltration in the central Southern Alps*. (Ph.D. thesis). New Zealand.
- Peltzer, G., Crampé, F., & King, G. (1999). Evidence of nonlinear elasticity of the crust from the Mw 7. 6 Manyi (Tibet) earthquake. *Science*, 286(5438), 272–276. <https://doi.org/10.1126/science.286.5438.272>
- Qin, Z., Fu, H., & Chen, X. (2019). A study on altered granite meso-damage mechanisms due to water invasion-water loss cycles. *Environmental Earth Sciences*, 78(14), 428. <https://doi.org/10.1007/s12665-019-8426-6>
- Rajendran, K., Rajendran, C. P., Jain, S. K., Murty, C. V. R., & Arlekar, J. N. (2000). The Chamoli earthquake, Garhwal Himalaya: Field observations and implications for seismic hazard. *Current Science*, 78(1), 45–51.
- Rosen, P. A., Gurrola, E., Sacco, G. F., & Žebeková, H. (2012). The InSAR scientific computing environment. In *EUSAR 2012; 9th European conference on synthetic aperture radar* (pp. 730–733). VDE.
- Saleh, M., Masson, F., Mohamed, A. M. S., Boy, J. P., Abou-Aly, N., & Rayan, A. (2018). Recent ground deformation around lake Nasser using GPS and InSAR, Aswan, Egypt. *Tectonophysics*, 744, 310–321. <https://doi.org/10.1016/j.tecto.2018.07.005>
- Sharma, N., & Prasad, R. (2018). Geological and geotechnical evaluation for the stabilization of tail race tunnel outfall slope – A case study of Tehri pump storage plant (1000 MW), Tehri Garhwal (Uttarakhand). *Fluid Mechanics Research International Journal*, 2(5), 234–241. <https://doi.org/10.15406/fmrij.2018.02.00043>
- Silverii, F., d'Agostino, N., Métois, M., Fiorillo, F., & Ventafridda, G. (2016). Transient deformation of karst aquifers due to seasonal and multiyear groundwater variations observed by GPS in southern Apennines (Italy). *Journal of Geophysical Research: Solid Earth*, 121(11), 8315–8337. <https://doi.org/10.1002/2016jb013361>
- Silverii, F., Montgomery-Brown, E. K., Borsa, A. A., & Barbour, A. J. (2020). Hydrologically induced deformation in Long Valley Caldera and Adjacent Sierra Nevada. *Journal of Geophysical Research: Solid Earth*, 125(5), e2020JB019495. <https://doi.org/10.1029/2020JB019495>
- Sima, S., & Tajrishy, M. (2013). Using satellite data to extract volume-area-elevation relationships for Urmia Lake, Iran. *Journal of Great Lakes Research*, 39(1), 90–99. <https://doi.org/10.1016/j.jglr.2012.12.013>
- Stevens, V. L., & Avouac, J. P. (2016). Millenary Mw > 9.0 earthquakes required by geodetic strain in the Himalaya. *Geophysical Research Letters*, 43(3), 1118–1123. <https://doi.org/10.1002/2015gl067336>
- Styron, R. H., & Hetland, E. A. (2015). The weight of the mountains: Constraints on tectonic stress, friction, and fluid pressure in the 2008 Wenchuan earthquake from estimates of topographic loading. *Journal of Geophysical Research: Solid Earth*, 120(4), 2697–2716. <https://doi.org/10.1002/2014jb011338>
- Tanaka, M., Girard, G., Davis, R., Peuto, A., & Bignell, N. (2001). Recommended table for the density of water between 0 C and 40 C based on recent experimental reports. *Metrologia*, 38(4), 301–309. <https://doi.org/10.1088/0026-1394/38/4/3>
- Tong, X., Sandwell, D. T., & Smith-Konter, B. (2013). High-resolution interseismic velocity data along the San Andreas Fault from GPS and InSAR. *Journal of Geophysical Research: Solid Earth*, 118(1), 369–389. <https://doi.org/10.1029/2012jb009442>
- van Dam, T., Wahr, J., Milly, P. C. D., Shmakin, A. B., Blewitt, G., Lavallée, D., & Larson, K. M. (2001). Crustal displacements due to continental water loading. *Geophysical Research Letters*, 28(4), 651–654. <https://doi.org/10.1029/2000gl012120>
- Wahr, J., Khan, S. A., Van Dam, T., Liu, L., Van Angelen, J. H., Van Den Broeke, M. R., & Meertens, C. M. (2013). The use of GPS horizontals for loading studies, with applications to northern California and southeast Greenland. *Journal of Geophysical Research: Solid Earth*, 118(4), 1795–1806. <https://doi.org/10.1002/jgrb.50104>
- Wahr, J., Smeed, D. A., Leuliette, E., & Swenson, S. (2014). Seasonal variability of the Red Sea, from satellite gravity, radar altimetry, and in situ observations. *Journal of Geophysical Research: Oceans*, 119(8), 5091–5104. <https://doi.org/10.1002/2014jc010161>
- Wang, R., & Kümpel, H. J. (2003). Poroelasticity: Efficient modeling of strongly coupled, slow deformation processes in multilayered half-space. *Geophysics*, 68(2), 705–717. <https://doi.org/10.1190/1.1567241>
- Wauthier, C., Cayol, V., Kervyn, F., & d'Oreye, N. (2012). Magma sources involved in the 2002 Nyiragongo eruption, as inferred from an InSAR analysis. *Journal of Geophysical Research*, 117(B5), B05411. <https://doi.org/10.1029/2011jb008257>
- Wei, M., & Sandwell, D. T. (2010). Decorrelation of L-band and C-band interferometry over vegetated areas in California. *IEEE Transactions on Geoscience and Remote Sensing*, 48(7), 2942–2952. <https://doi.org/10.1109/tgrs.2010.2043442>
- Xu, L. H., Liu, S. M., & Li, Y. Q. (2008). Experimental studies on rock softening properties in Danjiangkou Reservoir area. *Rock and Soil Mechanics*, 29(5), 1430–1434.
- Xu, W., Bürgmann, R., & Li, Z. (2016). An improved geodetic source model for the 1999 Mw 6.3 Chamoli earthquake, India. *Geophysical Journal International*, 205(1), 236–242. <https://doi.org/10.1093/gji/ggw016>
- Xu, W., Wu, S., Materna, K., Nadeau, R., Floyd, M., Funning, G., et al. (2018). Interseismic ground deformation and fault slip rates in the greater San Francisco Bay Area from two decades of space geodetic data. *Journal of Geophysical Research: Solid Earth*, 123(9), 8095–8109. <https://doi.org/10.1029/2018jb016004>
- Yadav, R. K., Gahalaut, V. K., Bansal, A. K., Sati, S. P., Catherine, J., Gautam, P., & Kumar, N. (2019). Strong seismic coupling underneath Garhwal–Kumaun region, NW Himalaya, India. *Earth and Planetary Science Letters*, 506, 8–14. <https://doi.org/10.1016/j.epsl.2018.10.023>

- Yang, X., Wang, J., Hou, D., Zhu, C., & He, M. (2018). Effect of dry-wet cycling on the mechanical properties of Rocks: A laboratory-scale experimental study. *Processes*, 6(10), 199. <https://doi.org/10.3390/pr6100199>
- Zhang, G., Chen, W., Li, G., Yang, W., Yi, S., & Luo, W. (2020). Lake water and glacier mass gains in the northwestern Tibetan Plateau observed from multi-sensor remote sensing data: Implication of an enhanced hydrologic cycle. *Remote Sensing of Environment*, 237, 111554. <https://doi.org/10.1016/j.rse.2019.111554>
- Zhang, L. (2017). Evaluation of rock mass deformability using empirical methods—A review. *Underground Space*, 2(1), 1–15. <https://doi.org/10.1016/j.undsp.2017.03.003>
- Zhao, B., Bürgmann, R., Wang, D., Tan, K., Du, R., & Zhang, R. (2017). Dominant controls of downdip afterslip and viscous relaxation on the postseismic displacements following the Mw7.9 Gorkha, Nepal, earthquake. *Journal of Geophysical Research: Solid Earth*, 122(10), 8376–8401. <https://doi.org/10.1002/2017JB014366>
- Zhao, J. J., Xie, M. L., Li, T., Tan, S.Y., Ju, N.P., & Bu, F. (2017). Softening effect of phyllite with water saturation. *Journal of Engineering Geology*, 25(6), 1449–1454.
- Zhao, W., Amelung, F., Dixon, T. H., Wdowinski, S., & Malservisi, R. (2014). A method for estimating ice mass loss from relative InSAR observations: Application to the Vatnajökull ice cap, Iceland. *Geochemistry, Geophysics, Geosystems*, 15(1), 108–120. <https://doi.org/10.1002/2013gc004936>
- Zhao, W., Amelung, F., Doin, M. P., Dixon, T. H., Wdowinski, S., & Lin, G. (2016). InSAR observations of lake loading at Yangzhuoyong Lake, Tibet: Constraints on crustal elasticity. *Earth and Planetary Science Letters*, 449, 240–245. <https://doi.org/10.1016/j.epsl.2016.05.044>
- Zhao, Z., Yang, J., Zhang, D., & Peng, H. (2017). Effects of wetting and cyclic wetting–drying on tensile strength of sandstone with a low clay mineral content. *Rock Mechanics and Rock Engineering*, 50(2), 485–491. <https://doi.org/10.1007/s00603-016-1087-9>